

# FIRST OBSERVATIONAL SIGNATURE OF ROTATIONAL DECELERATION IN A MASSIVE, INTERMEDIATE-AGE STAR CLUSTER IN THE MAGELLANIC CLOUDS

XIAOHAN WU<sup>1,2</sup>, CHENGYUAN LI<sup>2,3,4,5</sup>, RICHARD DE GRIJS<sup>2,6</sup>, AND LICAI DENG<sup>3</sup>

<sup>1</sup>School of Physics, Peking University, Yi He Yuan Lu 5, Hai Dian District, Beijing 100871, China

<sup>2</sup>Kavli Institute for Astronomy & Astrophysics and Department of Astronomy, Peking University, Yi He Yuan Lu 5, Hai Dian District, Beijing 100871, China; grijs@pku.edu.cn

<sup>3</sup>Key Laboratory for Optical Astronomy, National Astronomical Observatories, Chinese Academy of Sciences, 20A Datun Road, Chaoyang District, Beijing 100012, China

<sup>4</sup>Department of Physics and Astronomy, Macquarie University, Sydney, NSW 2109, Australia

<sup>5</sup>Purple Mountain Observatory, Chinese Academy of Sciences, Nanjing 210008, China

<sup>6</sup>International Space Science Institute–Beijing, 1 Nanertiao, Zhongguancun, Hai Dian District, Beijing 100190, China

## ABSTRACT

While the extended main-sequence turn-offs (eMSTOs) found in almost all 1–2 Gyr-old star clusters in the Magellanic Clouds are often explained by postulating extended star-formation histories, the tight subgiant branches (SGBs) seen in some clusters challenge this popular scenario. Puzzlingly, the SGB of the eMSTO cluster NGC 419 is significantly broader at bluer than at redder colors. We carefully assess and confirm the reality of this observational trend. If we would assume that the widths of the features in color–magnitude space were entirely owing to a range in stellar ages, the star-formation histories of the eMSTO stars and the blue SGB region would be significantly more prolonged than that of the red part of the SGB. This cannot be explained by assuming an internal age spread. We show that rotational deceleration of a population of rapidly rotating stars, a currently hotly debated alternative scenario, naturally explains the observed trend along the SGB. Our analysis shows that a ‘converging’ SGB could be produced if the cluster is mostly composed of rapidly rotating stars that slow down over time owing to the conservation of angular momentum during their evolutionary expansion from main-sequence turn-off stars to red giants.

*Keywords:* galaxies: star clusters: individual (NGC 419) — Hertzsprung-Russell and C-M diagrams — Magellanic Clouds — stars: rotation

## 1. INTRODUCTION

The once common perception that the member stars of most star clusters originate from ‘simple stellar populations’ (SSPs) is increasingly challenged by discoveries of extended main-sequence turn-offs (eMSTOs) in the color–magnitude diagrams (CMDs) of intermediate-age, 1–2 Gyr-old massive star clusters in the Magellanic Clouds (e.g., Mackey & Broby Nielsen 2007; Mackey et al. 2008; Milone et al. 2009; Rubele et al. 2010; Girardi et al. 2013; Li et al. 2014a). If solely interpreted in terms of stellar age distributions, such eMSTOs may imply age spreads greater than 300 Myr (e.g., Rubele et al. 2010, 2011; Goudfrooij et al. 2014). However, this strongly contradicts our current understanding of the evolution of SSP-like star clusters, whose maximum age spreads are expected to reach only 1–3 Myr (Longmore et al. 2014).

Li et al. (2014b) were the first to focus on the subgiant-branch (SGB) morphology of an eMSTO cluster, NGC 1651. Its tight SGB is inconsistent with the presence of a significant age spread. Simultaneously, Bastian & Niederhofer (2015) discovered that the SGB and red clump morphologies of two other intermediate-age star clusters, NGC 1806 and NGC 1846, also favor SSP scenarios. Several authors have shown that the presence of a range of stellar rotation rates in a single-age stellar population can produce the observed eMSTO features (e.g., Bastian & de Mink 2009; Yang et al. 2013; Brandt & Huang 2015; Niederhofer et al. 2015). In addition, a sufficiently low mixing efficiency could generate a tight SGB, resembling the observed SGB morphologies (Yang et al. 2013). Recently, the stellar rotation scenario received further support from Milone et al. (2016), who discovered that the split main sequences in the young Large Magellanic Cloud cluster NGC 1755 could best be explained by stellar rotation, and not by adopting an age

spread.

Here we report the discovery of a ‘converging’ SGB in the Small Magellanic Cloud eMSTO star cluster NGC 419: its SGB is significantly broader on the blue than on the red side. The apparently prolonged star-formation histories (SFHs) implied by the eMSTO stars and the blue region of the SGB contradict that derived for the red SGB region. We conclude that the observed SGB morphology can be explained by rotational deceleration owing to the conservation of angular momentum during the evolutionary expansion of SGB stars.

## 2. DATA REDUCTION

We used archival images from *Hubble Space Telescope* (*HST*) program GO-10396 (PI: J. S. Gallagher), which employed the Advanced Camera for Surveys (ACS)/Wide Field Channel (WFC). The individual images in the F555W and F814W filters cover  $200'' \times 200''$ , offset by  $37''$  from the cluster center. The F555W and F814W filters closely resemble the Johnson–Cousins  $V$  and  $I$  bands, respectively. We downloaded four images with total exposure times of 1984 s and 1896 s in the F555W ( $V$ ) and F814W ( $I$ ) filters, respectively, as well as two images with total exposure times of 40 s and 20 s in these filters. To facilitate field-star decontamination, we also retrieved images of a nearby field region at some  $230''$  from the cluster center, observed as part of the same *HST* program with the same instrumental setup. The latter observations, covering the same total area on the sky, include three images with total exposure times of 1617 s and 1512 s and one image each with exposure times of 50 s and 48 s in the  $V$  and  $I$  bands, respectively.

We performed point-spread-function (PSF) photometry using both IRAF/DAOPHOT (Davis 1994) and DOLPHOT’s ACS module (Dolphin 2011, 2013). We adopted the DOLPHOT stellar catalog for our analysis and used the IRAF/DAOPHOT photometry for comparison and consistency checks (see Appendix). We determined the cluster center by fitting Gaussian functions to the cluster’s number-density profiles along the right ascension ( $\alpha_{J2000}$ ) and declination ( $\delta_{J2000}$ ) axes:  $\alpha_{J2000} = 01^{\text{h}}08^{\text{m}}17.02^{\text{s}}$ ,  $\delta_{J2000} = -72^{\circ}53'3.12''$ . This center position compares very well with previous determinations.<sup>1</sup> We obtained the cluster radius,  $R$ , based on Elson et al. (1987, EFF) profile fits (appropriate for non-tidally truncated clusters) to the completeness-corrected projected radial stellar number density, adopting for the cluster radius five times its core radius, i.e.,  $R = 75''$  (see Appendix).

Next, we performed statistical field-star decontamination. We divided the cluster and field CMDs into 15 bins along the color axis,  $-1.0 \leq (V - I) \leq 3.0$  mag, and 28 bins along the magnitude axis,  $16.0 \leq V \leq 27.0$  mag. We measured the number of field stars in each bin in the field CMD and randomly removed the appropriate number—scaled by the ratio of the area within  $R = 75''$  to the total area covered by the field CMD—from the corresponding bin of the cluster CMD. If the number of stars that had to be removed was larger than the number of stars present in a given bin, all stars were removed. To ascertain the reliability of this approach, we also employed a method similar to that of Cabrera-Ziri et al. (2016), which showed that the SGB region is characterized by a ‘signal-to-noise ratio’  $\geq 35$  (see Appendix). We confirmed that changing the color  $\times$  magnitude bin sizes from  $0.2 \times 0.3$  mag<sup>2</sup> to  $0.4 \times 0.5$  mag<sup>2</sup> yields similar results. The cleaned stellar catalog contains 17,346 stars with  $V \leq 27.0$  mag.

## 3. MAIN RESULTS

Figure 1 shows the NGC 419 CMD after field-star decontamination. The cluster has an eMSTO at  $20 \leq V \leq 22$  mag. We adopted the Padova stellar evolution models (PARSEC CMD 2.7, v. 1.2S; Bressan et al. 2012),<sup>2</sup> for  $Z = 0.004$  (Girardi et al. 2009; Glatt et al. 2008), and fitted the eMSTO extremes with isochrones of  $\log(t \text{ yr}^{-1}) = 9.12$  (1.32 Gyr; blue line) and  $\log(t \text{ yr}^{-1}) = 9.31$  (2.02 Gyr; red line), adopting a distance modulus,  $(m - M)_0 = 18.90$  mag and a visual extinction  $A_V = 0.181$  mag (Rubele et al. 2010). The maximum possible age spread implied by the extent of the eMSTO is  $\sim 700$  Myr, similar to the results of Rubele et al. (2010,  $\sim 700$  Myr) and Girardi et al. (2013,  $\sim 670$  Myr). However, the cluster exhibits a SGB that is broad on the blue side and which becomes significantly narrower on the red side. Previous studies of intermediate-age star clusters with eMSTOs usually showed tight SGBs throughout (Mackey & Broby Nielsen 2007; Li et al. 2014b; Bastian & Niederhofer 2015) (but see Goudfrooij et al. 2015). This feature is, however, already apparent in the NGC 419 data before field-star decontamination and is, hence, not caused by our data reduction. In addition, the significance level of our field-star decontamination is very high along the SGB, while the good agreement between our IRAF/DAOPHOT and DOLPHOT stellar catalogs further confirms the reality of the SGB morphology. Examination of the SGB stars’ spatial distribution reveals that blending is unlikely responsible for the observed narrowing either. The NGC 419 CMD of Goudfrooij et al. (2014) shows a similar trend, although that of Glatt et al. (2008) resembles an SSP more closely. The latter CMD is, however, composed of *HST* ACS/High

<sup>1</sup> <http://ned.ipac.caltech.edu/cgi-bin/objsearch?objname=ngc+419>, <http://simbad.u-strasbg.fr/simbad/sim-basic?Ident=ngc+419>.

<sup>2</sup> <http://stev.oapd.inaf.it/cgi-bin/cmd.2.7>

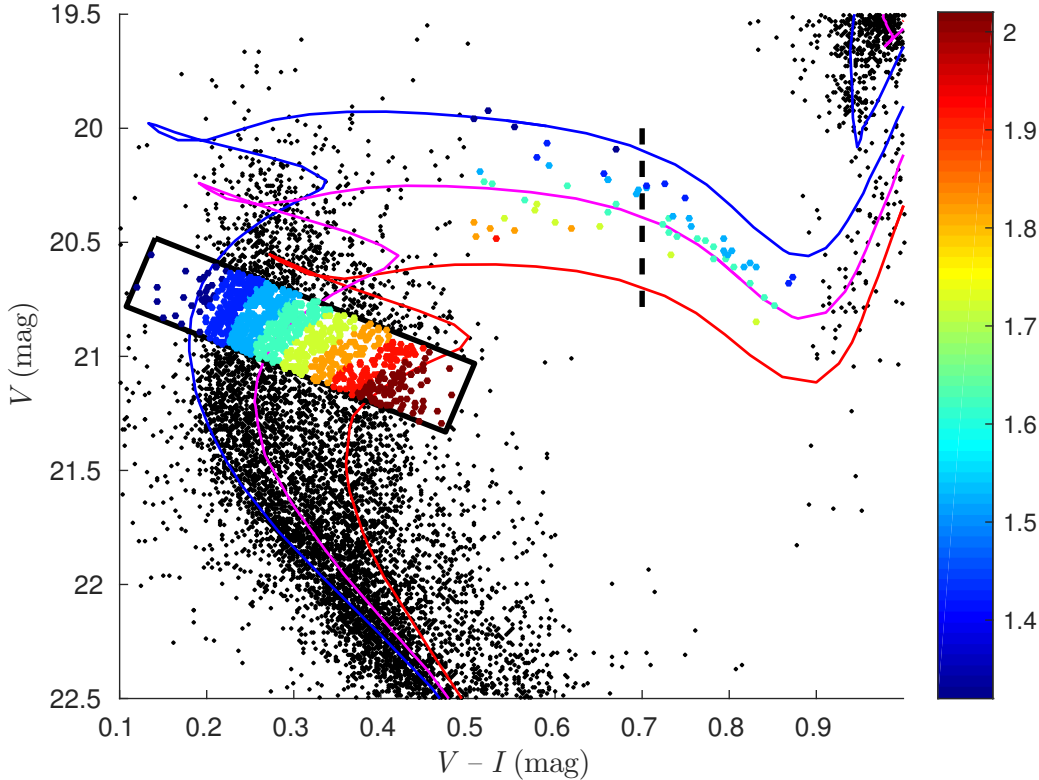


**Figure 1.** NGC 419 CMD, showing isochrones of 1.32 Gyr (blue), 1.52 Gyr (magenta; corresponding to the peak in the cluster’s SFH based on its red SGB morphology), and 2.02 Gyr (red). Colored points are the SGB stars and the eMSTO stars used to derive the SFHs (black box), assuming that these features can be described solely by stellar age ranges (indicated by the color bar; in Gyr). The vertical dashed black line shows where we separate the SGB stars into blue and red samples.

Resolution Channel observations covering a small stellar sample located in the cluster’s central region only. Our data are consistent with the [Glatt et al. \(2008\)](#) CMD for stars drawn from inside the cluster’s core radius. We thus conclude that the observed narrowing of the NGC 419 SGB is real and not caused by artifacts associated with our data reduction (see Appendix).

To characterize the narrowing of the SGB, we derived SFHs based on the morphologies of the blue and red sides of the SGB. We first selected SGB stars at  $0.50 \leq (V - I) \leq 0.89$  mag, where the blue boundary is the red boundary of the eMSTO (determined by the oldest isochrone used), while at the red boundary the model SGB luminosity reaches a minimum. We divided the full sample into blue and red subsamples at  $(V - I) = 0.7$  mag. The blue SGB stars span a broad range in luminosity, while on the red side almost all SGB stars converge to a significantly narrower distribution. For each SGB star we determined the best-fitting isochrone, adopting isochrones from 1.32 Gyr to 2.02 Gyr, in steps of 100 Myr. We counted the fractions of SGB stars pertaining to each isochrone to derive the SGB’s SFHs. The SGB lifetime is a monotonically increasing function of the isochrone age adopted, ranging from 9 Myr for the 1.32 Gyr isochrone to 22 Myr for the 2.02 Gyr isochrone ([Bressan et al. 2012](#)), i.e., significantly shorter than our age resolution of 100 Myr. The small range in SGB lifetimes therefore does not affect the SFHs derived. In addition, the probability of an SGB star to be associated with a given isochrone is nearly the same for all ages.

Typical uncertainties in our SGB photometry are very small ( $\Delta V \leq 0.040$  mag,  $\Delta I \leq 0.044$  mag), corresponding to a  $\lesssim 50$  Myr age uncertainty. The isochrone fits are therefore well-constrained. We averaged the SFHs derived from the catalogs of 100 field-star decontamination runs to minimize the effects of randomly removing stars. The average numbers of blue and red SGB stars are both 31. Figure 2 shows the SFHs derived for the blue and red SGB subsamples. The former is clearly much flatter and more extended than the latter, which is characterized by a sharp peak at 1.62 Gyr (see the magenta isochrone in Fig. 1) and falls off steeply on either side. The ratios of the periods stars spend in the red versus blue SGB regions are approximately the same for all adopted ages,  $\sim 1.3$  ([Bressan et al. 2012](#)). Hence, our derived SFHs reliably represent the real SFHs. Note that while the apparently broadened base of the red-giant branch (RGB) in the CMD is affected by lingering contamination by field RGB stars owing to statistical

fluctuations in the small numbers of RGB cluster and field stars, field contamination does not affect the morphology of the SGB to the same extent.

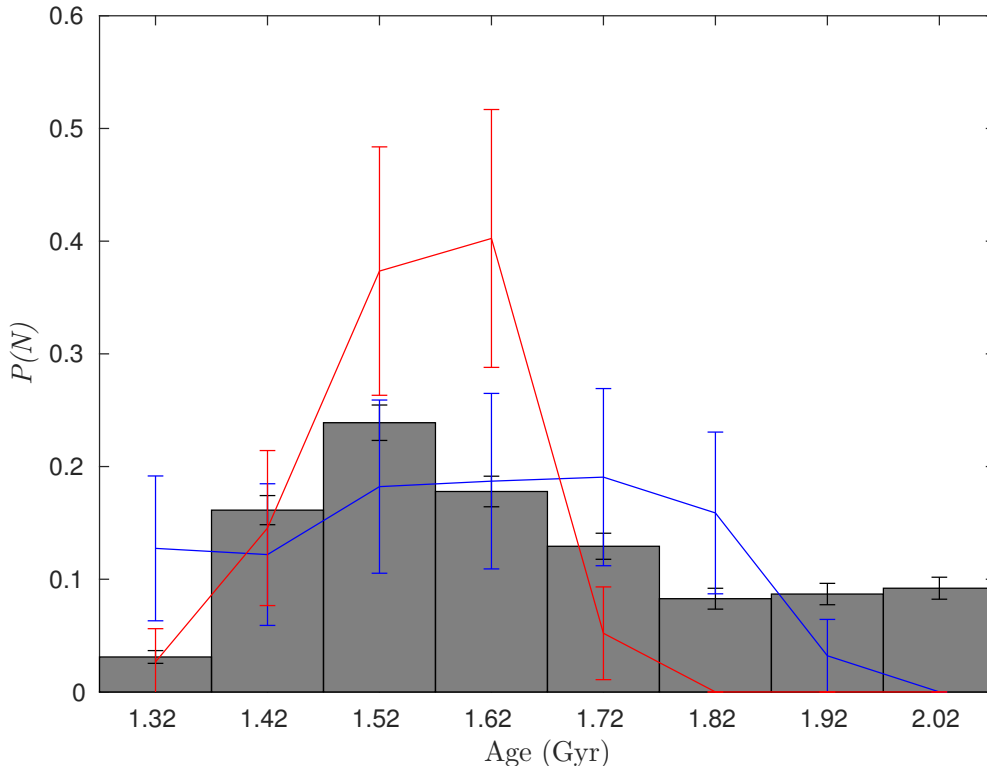


**Figure 2.** SFHs derived from our sample SGB and eMSTO stars. Blue, red lines: SFHs of the blue, red sample SGB stars, respectively. Gray histogram: SFH of the eMSTO stars. The error bars represent  $1\sigma$  Poissonian uncertainties.

We next derived the most representative eMSTO SFH. We first selected a representative eMSTO sample, shown as the black box in Fig. 1. Its left- and right-hand boundaries run approximately parallel to the isochrones, while the top and bottom boundaries are oriented perpendicularly to the isochrones. Our selection was made such that the isochrones are well separated from each other, while the influence of binary stars is minimized (e.g., Goudfrooij et al. 2014). For each of our 967 eMSTO stars, we determined the best-fitting isochrone, using the same isochrone set as for our SGB analysis. Figure 2 shows the SFH derived for the eMSTO (gray histogram), indicating an age spread from 1.32 Gyr to 2.02 Gyr. In the presence of small-number statistical fluctuations, this may be consistent with the SFH resulting from the blue part of the SGB region, but certainly not with its red SFH. We constructed 1000 synthetic clusters characterized by the eMSTO’s SFH to check whether the lack of old red SGB stars could have been caused by stochastic effects. The results imply that the ‘convergence’ of the NGC 419 SGB is unlikely caused by stochastic sampling; for instance, the probability of detecting fewer than 10% of the red SGB stars near the oldest isochrones is  $P < 0.05$ . This hence raises significant doubts as to the presence of a genuine age spread in the cluster. It is thus essential to consider alternative explanations for the observed variation in the NGC 419 SGB morphology.

#### 4. DISCUSSION

A significant number of recent papers have focused on the presence of rapidly rotating stars as a possible explanation of the observed eMSTOs (Bastian & de Mink 2009; Yang et al. 2013; Li et al. 2014a,b; Brandt & Huang 2015; Niederhofer et al. 2015). Stellar rotation affects the eMSTO area in two main ways, i.e., through gravity darkening and rotational mixing. Gravity darkening leads to luminosity and surface-temperature reductions owing to the centrifugal force, which enlarges the eMSTO area. Rotational mixing causes an increase in the sizes of the stellar convective cores, which prolongs the main-sequence lifetime and can counteract the effects of rotational mixing on the SGB. However, Yang et al. (2013) pointed out that stellar rotation could explain the origin of eMSTOs if a moderate rotational mixing

efficiency is adopted (see also Brandt & Huang 2015; Niederhofer et al. 2015). Li et al. (2014b) concluded that the tight SGB in NGC 1651 could be explained by a population of rapidly rotating stars if gravity darkening were dominant.

For NGC 419, we suspected that the converging trend along its SGB may be explained by rotational deceleration. Conservation of angular momentum implies that the expansion of SGB stars may eventually result in identical rotational evolution of both rapidly and slowly rotating stars. We used the Geneva stellar rotation models (Ekström et al. 2012; Georgy et al. 2013)<sup>3</sup> to explore whether the deceleration of rapid rotators can plausibly explain the SGB morphology of NGC 419.

We acquired four synthetic clusters, two characterized by a metallicity of  $Z = 0.002$  and the other two for  $Z = 0.006$ . For each metallicity we modeled one cluster with a flat initial rotation distribution and another with its initial rotation distribution based on Huang et al. (2010). We explored the effects of stellar rotation for B-type stars with nine different rotation rates,  $\Omega_{\text{ini}}/\Omega_{\text{crit}} = 0.0, 0.1, 0.2, 0.3, 0.4, 0.5, 0.6, 0.7, 0.8, 0.9$ , and  $0.95$ ;  $\Omega_{\text{ini}}$  is the initial stellar surface angular velocity and  $\Omega_{\text{crit}}$  is the critical or ‘break-up’ angular velocity (Georgy et al. 2013). All synthetic clusters have the same age,  $\log(t \text{ yr}^{-1}) = 9.1$ , i.e., the oldest available age for B-type stars (with masses  $m_* \geq 1.7M_{\odot}$ ) and the closest model age to that of NGC 419.

Figure 3 (left) shows the MSTO and SGB CMD regions for the two synthetic clusters with flat initial rotation distributions; the color bar represents  $\Omega/\Omega_{\text{crit}}$  at  $\log(t \text{ yr}^{-1}) = 9.1$ . We adopted the same  $A_V$  and distance modulus as for NGC 419 and implemented realistic photometric uncertainties. Fits of non-rotating Geneva isochrones to these eMSTOs imply age spreads of  $\sim 630$  Myr and  $\geq 460$  Myr for  $Z = 0.002$  and  $Z = 0.006$ , respectively.<sup>4</sup> Although the left-hand panels of Fig. 3 seem to suggest that none of the SGBs in our synthetic clusters converge into narrow sequences on the red side, it appears that the rapid rotators might converge into a narrower sequence, while the slow rotators occupy a much broader luminosity range.

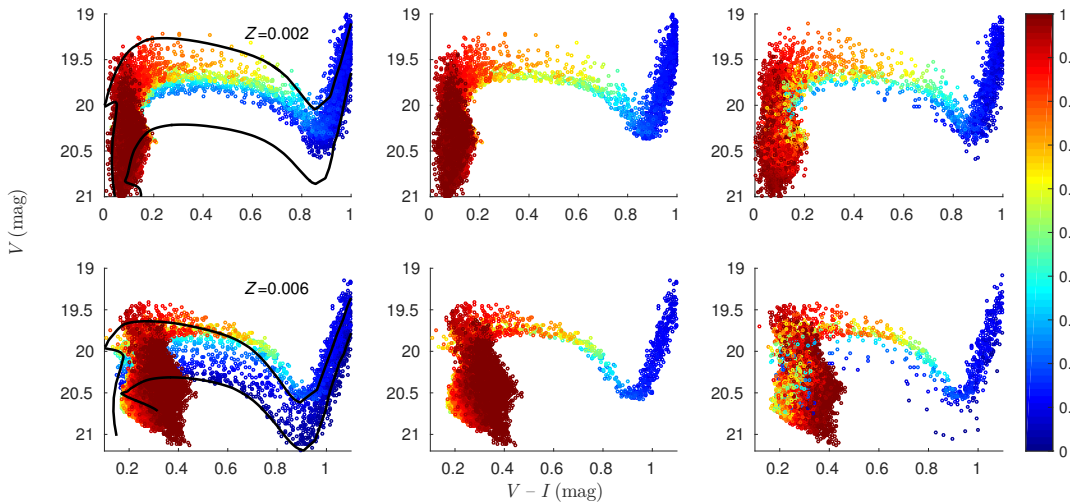


**Figure 3.** Synthetic cluster CMDs based on the Geneva stellar rotation models for (top)  $Z = 0.002$  and (bottom)  $Z = 0.006$ . Left: Adopting a flat initial rotation distribution,  $\Omega_{\text{ini}}/\Omega_{\text{crit}} \in [0, 1]$ . Color bar:  $\Omega/\Omega_{\text{crit}}$  at  $\log(t \text{ yr}^{-1}) = 9.1$ . Black lines:  $Z = 0.002$ , non-rotating isochrones for  $\log(t \text{ yr}^{-1}) = 8.8$  and  $\log(t \text{ yr}^{-1}) = 9.1$ ;  $Z = 0.006$ , non-rotating isochrones for  $\log(t \text{ yr}^{-1}) = 8.9$  and  $\log(t \text{ yr}^{-1}) = 9.1$ . Middle: As the left panels, but for a minimum at  $\Omega_{\text{ini}}/\Omega_{\text{crit}} = 0.5$ . Right: As the left panels, but for the initial rotation distribution of Huang et al. (2010). Note that the  $V$  and  $I$  magnitudes in the Geneva models refer to the Johnson–Cousins photometric system.

Hence we implemented a series of cut-offs to the initial rotation rates to explore the effects of varying the minimum  $\Omega_{\text{ini}}/\Omega_{\text{crit}}$  rate on the SGB morphology. Huang et al. (2010) determined that most low-mass ( $2 < m_*/M_{\odot} < 4$ ) B-type stars are born as rapid rotators: the fraction of their slowly rotating sample stars, with rotation-velocity ratios  $V_{\text{eq}}/V_{\text{crit}} < 0.5$ , is 37%. We found that the convergence of the SGB is most evident for initially rapid rotators: see Fig. 3 (middle), where the CMDs are composed of stars with  $\Omega_{\text{ini}}/\Omega_{\text{crit}} > 0.5$ . The color bar represents  $\Omega/\Omega_{\text{crit}}$  at  $\log(t \text{ yr}^{-1}) = 9.1$ . Assessment of the colored data points also shows that the SGB stars on the red side of the CMDs

<sup>3</sup> <http://obswww.unige.ch/Recherche/evol/-Database->

<sup>4</sup> The lack of SGB stars along the non-rotating isochrone of  $\log \log(t \text{ yr}^{-1}) = 9.1$  in the  $Z = 0.002$  CMD is caused by the B-type stars with  $\Omega_{\text{ini}}/\Omega_{\text{crit}} \leq 0.3$  already having left the SGB.

have all slowed down to approximately the same  $\Omega/\Omega_{\text{crit}} \leq 0.3\text{--}0.4$  at  $\log(t \text{ yr}^{-1}) = 9.1$ .

The eMSTO stars in NGC 419 may be rotating faster than expected, given that the converging cluster SGB suggests that gravity darkening may indeed be important. Metallicity variations may also have a significant impact on stellar atmospheric convection. When rapid rotators are compared with slow rotators, rotational mixing dominates the SGB morphology, because slowly rotating stars occupy the bottom part of the SGB and broaden it to a large extent. However, the assumption of a cluster to contain only rapid rotators seems unrealistic. Nevertheless, the young clusters NGC 1856 (D’Antona et al. 2015) and NGC 1755 (Milone et al. 2016) both appear to consist of two-thirds of rapid rotators. Therefore, we explored synthetic CMDs based on the initial rotation distribution of Huang et al. (2010): see Fig. 3 (right). Note that at  $\log(t \text{ yr}^{-1}) = 9.1$ , all stars in the  $Z = 0.002$  CMD with  $\Omega_{\text{ini}}/\Omega_{\text{crit}} \leq 0.3$  will already have evolved off the SGB. However, the  $Z = 0.006$  cluster clearly shows that the initially rapid rotators outnumber their (initially) slowly rotating counterparts. The probability of finding initially rapid rotators along real cluster SGBs is, therefore, much higher than that for slow rotators. In addition, initially slowly rotating SGB stars in the  $Z = 0.006$  CMD are faint. If such stars are present in the NGC 419 CMD, they may be mixed with field stars and, hence, will have been removed. It is therefore likely that NGC 419 is indeed composed of a large fraction of rapid rotators. Unfortunately, it is still cumbersome to model synthetic clusters with metallicities other than  $Z = 0.002$ ,  $Z = 0.006$ , and  $Z = 0.014$ , or ages  $\log(t \text{ yr}^{-1}) > 9.1$ . Therefore, the effects of stellar rotation on the SGB morphology of real star clusters are still tentative. Published CMDs also suggest that NGC 1852 (Goudfrooij et al. 2014), NGC 2154 (Goudfrooij et al. 2014; Milone et al. 2009), NGC 2203 (Goudfrooij et al. 2014), and Hodge 7 (Milone et al. 2009) may exhibit similar converging trends along their SGBs, although somewhat less obvious than that in NGC 419.

## 5. SUMMARY AND CONCLUSIONS

We obtained PSF photometry from archival *HST* images of the Small Magellanic Cloud star cluster NGC 419 using two independent software packages, IRAF/DAOPHOT and DOLPHOT. The CMDs resulting from both stellar catalogs are mutually consistent and show a narrowing trend along the cluster’s SGB, i.e., the NGC 419 SGB appears to be significantly narrower at redder than at bluer colors.

Initially assuming, for simplicity and in line with previous work, that the widths of our CMD features may be driven entirely by stellar age distributions, we derived SFHs using a sample of eMSTO stars, as well as stars on the blue and red sides of the cluster’s SGB. The SFH for the red SGB exhibits a sharp peak at an age of 1.52 Gyr and drops off steeply on either side of the peak, while the blue SGB morphology is consistent with a much larger age range, from 1.32 Gyr to 1.92 Gyr. Moreover, the SFH of the eMSTO stars suggests an even broader age range, from 1.32 Gyr to 2.02 Gyr. These three independently derived SFHs challenge the postulated presence of a significant age spread to explain the observed eMSTO extent. Hence, we considered the presence of a population of stars with different stellar rotation rates.

For a synthetic cluster of age  $\log(t \text{ yr}^{-1}) = 9.1$  and  $Z = 0.002$  or  $Z = 0.006$ , the SGB’s convergence is most prominent for stars with  $\Omega_{\text{ini}}/\Omega_{\text{crit}} > 0.5$ , which suggests that NGC 419 may be composed of a large fraction of rapidly rotating stars. Future improvements of stellar rotation models are urgently needed to reach robust conclusions as to the importance of variations in stellar rotation rates in intermediate-age star clusters.

## ACKNOWLEDGEMENTS

We thank Yi Hu for his assistance with the DOLPHOT photometry and with processing of the stellar catalogs. X. H. W. is grateful for support from Peking University’s Junzheng Fund for Undergraduate Research. C. L. is partially supported by Strategic Priority Program ‘The Emergence of Cosmological Structures’ of the Chinese Academy of Sciences (grant XDB09000000) and by a Macquarie Research Fellowship. R. d. G. and L. D. acknowledge research support from the National Natural Science Foundation through grants 11073001, 11373010, and 11473037.

## REFERENCES

- |   |   |
|---|---|
| Bastian, N., & de Mink, S. E. 2009, MNRAS, 398, L11                           | D’Antona, F., Di Criscienzo, M., Decressin, T., et al. 2015, MNRAS, 453, 2637   |
| Brandt, T. D., & Huang, C. X. 2015, ApJ, 807, 25                              | Davis, L. E., A Reference Guide to the IRAF/DAOPHOT Package, <a href="http://iraf.noao.edu/iraf/web/docs/recommend.html">http://iraf.noao.edu/iraf/web/docs/recommend.html</a> , 1994 |
| Bastian, N., & Niederhofer, F. 2015, MNRAS, 448, 1863                         | Dolphin A., DOLPHOT/ACS user’s guide, version 2.0. <a href="http://americano.dolphinism.com/dolphin/dolphinACS.pdf">http://americano.dolphinism.com/dolphin/dolphinACS.pdf</a> , 2011 |
| Bressan, A., Marigo, P., Girardi, L., et al. 2012, MNRAS, 427, 127            |   |
| Cabrera-Ziri, I., Niederhofer, F., Bastian, N., et al. 2016, MNRAS, 459, 4218 |   |

- Dolphin A., DOLPHOT user’s guide, version 2.0.  
<http://americano.dolphinism.com/dolphin/dolphin.pdf>, 2013
- Ekström, S., Georgy, C., Eggenberger, P., et al. 2012, *A&A*, 537, A146
- Elson, R. A. W., Fall, S. M., & Freeman, K. C. 1987, *ApJ*, 323, 54
- Georgy, C., Ekström, S., Eggenberger, P., et al. 2013, *A&A*, 558, A103
- Girardi, L., Goudfrooij, P., Kalirai, J. S., et al. 2013, *MNRAS*, 431, 3501
- Girardi, L., Rubele, S., & Kerber, L. 2009, *MNRAS*, 394, L74
- Glatt, K., Grebel, E. K., Sabbi, E., et al. 2008, *AJ*, 136, 1703
- Goudfrooij, P., Girardi, L., Kozhurina-Platais, V., et al. 2014, *ApJ*, 797, 35
- Goudfrooij, P., Girardi, L., Rosenfield, P., et al. 2015, *MNRAS*, 450, 1693
- Huang, W., Gies, D. R., & McSwain, M. V. 2010, *ApJ*, 722, 605
- Kroupa, P. 2001, *MNRAS*, 322, 231
- Li, C., de Grijs, R., & Deng, L. 2014, *ApJ*, 784, 157
- Li, C., de Grijs, R., & Deng, L. 2014, *Nature*, 516, 367
- Longmore, S. N., Kruijssen, J. M. D., Bastian, N., et al. 2014, *Protostars and Planets VI*, 291
- Mackey, A. D., & Broby Nielsen, P. 2007, *MNRAS*, 379, 151
- Mackey, A. D., Broby Nielsen, P., Ferguson, A. M. N., & Richardson, J. C. 2008, *ApJL*, 681, L17
- Milone, A. P., Bedin, L. R., Piotto, G., & Anderson, J. 2009, *A&A*, 497, 755
- Milone, A. P., Marino, A. F., D’Antona, F., et al. 2016, *MNRAS*, 458, 4368
- Niederhofer, F., Georgy, C., Bastian, N., & Ekström, S. 2015, *MNRAS*, 453, 2070
- Rubele, S., Girardi, L., Kozhurina-Platais, V., Goudfrooij, P., & Kerber, L. 2011, *MNRAS*, 414, 2204
- Rubele, S., Kerber, L., & Girardi, L. 2010, *MNRAS*, 403, 1156
- Yang, W., Bi, S., Meng, X., & Liu, Z. 2013, *ApJ*, 776, 112

## APPENDIX

Here we introduce the details of our data reduction, including the determination of the cluster center, its radius, and the procedures used for field-star decontamination. We also summarize the matching, cleaning, and comparison of the DOLPHOT and IRAF/DAOPHOT stellar catalogs.

### DOLPHOT AND IRAF/DAOPHOT *PHOTOMETRY*

The DOLPHOT software generated one stellar catalog for each pair of images taken in the  $V$  and  $I$  bands, so that we have four initial stellar catalogs pertaining to the deep exposures and two stellar catalogs resulting from the shallower exposures. ‘Bad’ sources were removed following the prescriptions in the DOLPHOT manual (Dolphin 2013). We also referred to Mackey & Broby Nielsen (2007)’s data reduction of NGC 1846 when removing the ‘bad’ objects. The cleaned initial stellar catalogs only contain stars with  $-0.15 \leq \text{sharpness} \leq 0.15$ ,  $\text{crowding} \leq 0.5$ , and photometric errors  $\leq 0.2$  mag. We also only retained sources with object type 1, i.e., stars classified by DOLPHOT as ‘good.’ Next, we converted the stars’  $x$  and  $y$  positions on the images into right ascension and declination, using the python package DRIZZLEPAC, which corrects for astrometric image distortions. Using the stellar positions on the sky as the criterion for matching stars in different stellar catalogs, we combined the four long-exposure stellar catalogs into a single catalog, where we only selected those stars that appear in all four images. The stellar catalogs resulting from the shorter exposure times were similarly combined. Subsequently, we combined the deep and shallow stellar catalogs, since bright stars are saturated in the long exposures and faint stars cannot be detected in the short exposures. If a star appeared both in the long- and short-exposure catalogs, we included the photometry from the deeper observation. The same procedures were used to obtain the stellar catalog pertaining to the nearby background field.

As regards the IRAF/DAOPHOT photometry, the four long-exposure images were first aligned and combined into a single image. PSF photometry was then performed on the combined image, resulting in a single stellar catalog containing all  $V$ -band information and a second catalog containing the  $I$ -band photometry. We then applied a series of parameters to clean the two stellar catalogs, including cut-offs in the sharpness and in the number of iterations ( $n_{\text{iter}}$ ) it took to properly fit a star. Next, we matched the  $V$ - and  $I$ -band catalogs to assess the quality of the CMD. The final parameters adopted were sharpness  $\in [-0.3, 0.3]$ ,  $n_{\text{iter}} < 40$ , and photometric errors  $< 0.2$  mag. These ranges produced a CMD that is sufficiently ‘clean’ and a stellar catalog that is sufficiently complete for the purposes of this paper; limiting the sharpness value to a smaller range would remove too many stars.<sup>5</sup>

### ARTIFICIAL STAR TESTS

We performed artificial star tests using DOLPHOT to assess the spatially dependent completeness levels. We generated  $\sim 750,000$  fake stars, which we added to the raw images, and performed PSF photometry on these stars. To ensure that the fake stars did not significantly increase the crowding of the images, we only added 100 fake stars to an image at any time. After all artificial stars had been measured properly, we removed ‘bad’ sources using the same

<sup>5</sup> We also checked by comparison with the DOLPHOT stellar catalog what the effect would be of changing the range in sharpness value from  $[-0.15, 0.15]$  to  $[-0.3, 0.3]$ . This did not affect the SGB morphology.

criteria as adopted for removing ‘bad’ sources from the catalog of real cluster stars. Stars whose measured magnitudes differed more than 0.25 mag from their input magnitudes and those whose  $(x, y)$  positions on the images differed by more than 0.5 pixels from the input positions were considered to not have been recovered. Using these criteria, we obtained a catalog of ‘recovered’ fake stars. We next calculated the distance of each fake star to the cluster center (see below) and divided them into radial and magnitude bins. We used these bins, in turn, to calculate the fractions of the number of ‘recovered’ stars with respect to the original number of stars. These fractions represent the spatially dependent completeness levels, which we used in the determination of the cluster’s structural parameters. The full two-dimensional spatially dependent completeness surface is shown in Fig. 4 (left).

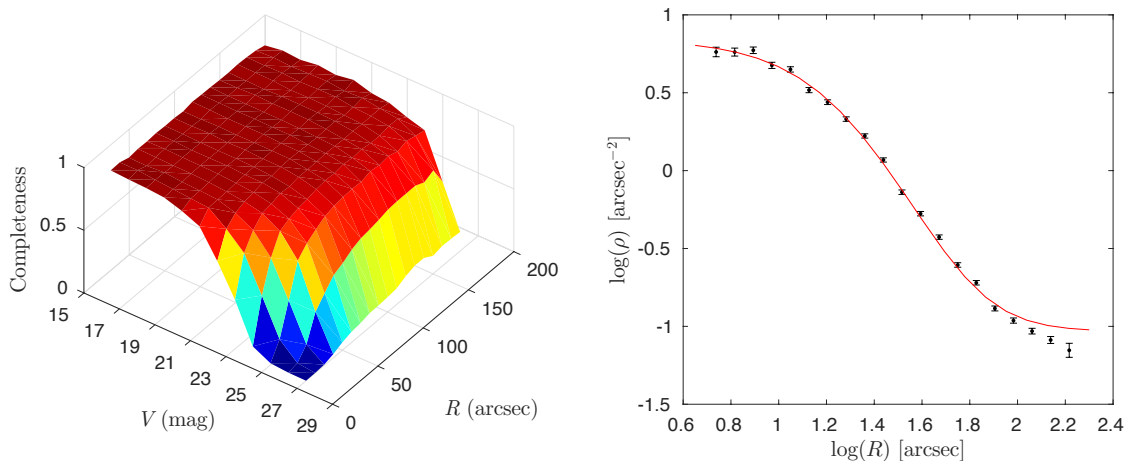


**Figure 4.** Left: Spatially dependent completeness levels as a function of cluster radius and stellar magnitude. Right: Completeness-corrected radial number-density profile of NGC 419. The  $1\sigma$  uncertainties are defined by Poissonian noise statistics. The red curve is the best-fitting EFF profile.

### CLUSTER STRUCTURE

We determined the cluster’s structural parameters by calculating the (projected) radial stellar number-density profile. To do so, we counted the numbers of stars in different rings,  $N(R)$ , and divided them by the areas of the rings,  $A(R)$ . The number of stars in each ring was corrected for the spatially dependent completeness. However, since the completeness level near the cluster center is lower than that in the outer regions, faint stars that can be detected in the outer parts cannot always be detected in the inner regions. Therefore, we only used stars brighter than  $V = 22.5$  mag when calculating the cluster’s number-density profile, because at this brightness the completeness curve of the innermost ring decreases to 50%.

The areas of the rings were estimated using a Monte Carlo-type method, because some of the rings are not completely covered by the observations. Specifically, we first calculated the total area of the region observed and then generated a million points, homogeneously distributed across the entire region. We then used the number fraction of points located



in each ring, multiplied by the total area of the full region to represent the area of each ring. The radial number-density profile,  $f(R)$ , is then obtained,  $f(R) = N(R)/A(R)$ . We repeated this process six times and averaged the resulting radial number-density profile to minimize the random errors introduced by the Monte Carlo method. The average radial number-density profile is shown in the right-hand panel of Fig. 4, where the data points are represented by black points. The error bars represent  $1\sigma$  Poissonian uncertainties.

Since NGC 419 is an intermediate-age star cluster, we used an EFF profile to fit its radial number-density profile,

$$f(r) = f_0(1 + r^2/a^2)^{-\gamma/2} + \phi, \quad (1)$$

where  $f_0$  is the central projected stellar density,  $a$  is a measure of the core radius, and  $\gamma$  is the power-law slope. The parameter  $\phi$  is added to represent background contamination. The results of our fits are  $f_0 = 8.88 \text{ arcsec}^{-2}$ ,  $a = 19.17''$ ,  $\gamma = 3.43$ , and  $\phi = 0.093 \text{ arcsec}^{-2}$ . The radius where the stellar number density drops to half the central value is the core radius:  $r_c = 15''$ . The cluster radius is defined as five times the core radius:  $R=75''$ . This radius is sufficiently large to select a relatively complete sample of SGB stars; adopting a cluster radius that is much larger will cause considerable contamination of the SGB region by field stars.

### SGB MORPHOLOGY CONFIRMATION

#### SGB MORPHOLOGY COMPARISON

The left-hand and middle panels of Fig. 5 show the CMDs of the cluster stars at  $R < 75''$  based on the DOLPHOT and IRAF/DAOPHOT catalogs, respectively. The converging trend along the SGB is indeed clearly visible prior to us having performed field-star decontamination. To confirm this trend, we first made comparisons between our two stellar catalogs. We show zoom-ins of the SGB regions in the CMDs of both catalogs in the insets of the left-hand and middle panels of Fig. 5, for stars located at  $R \leq 30''$ . We used a radius of twice the core radius for this check, because the number of SGB stars inside  $R_{\text{core}} = 15''$  is too small, while the converging trend also disappears for stars located inside the core radius. On the other hand, a radius that is too large can cause significant contamination by field stars. The SGB stars, with  $0.5 \leq (V - I) \leq 0.89 \text{ mag}$ , are shown as magenta squares in those insets of Fig. 5. We matched the two samples of SGB stars and averaged their magnitudes to quantify the effects of averaging on the SGB morphology.

Among the 54 SGB stars in the IRAF/DAOPHOT catalog and the 48 SGB stars in the DOLPHOT catalog, 38 stars were matched. The ‘average’ SGB for  $R \leq 30''$  is shown in the right-hand panel of Fig. 5, where the orange and green squares are the matched SGB and the magnitude-averaged SGB stars, respectively. It is clear that the converging trend exhibited by the SGB stars in the DOLPHOT stellar catalog does not change significantly, which strongly suggests that this feature is intrinsic and not an artifact introduced by our photometric analysis or our method of matching stars.

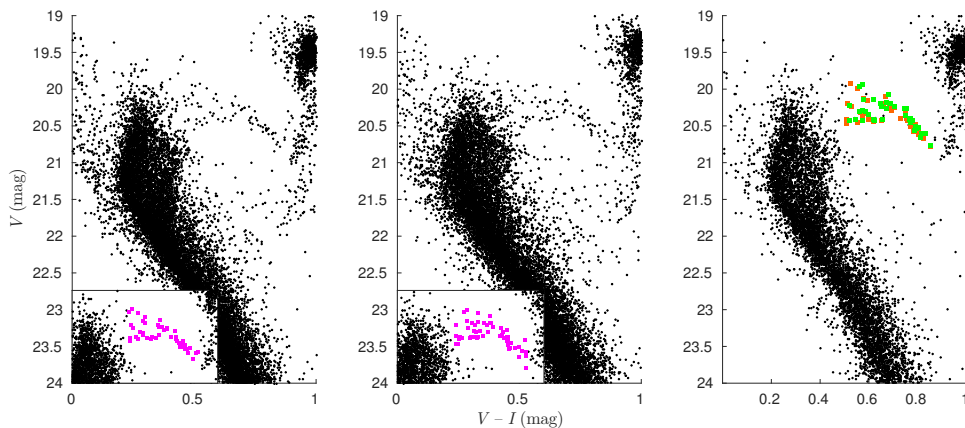


**Figure 5.** CMDs of NGC 419. Left, middle: based on the DOLPHOT, IRAF/DAOPHOT stellar catalogs for stars at  $R \leq 75''$ . Insets: SGB zoom-ins for stars within  $R = 30''$ . Magenta squares: SGB stars. Right: CMD of the stars within  $R = 30''$  from the DOLPHOT catalog. Orange squares: matched SGB stars from the DOLPHOT catalog. Green squares: magnitude-averaged, matched SGB stars.

*FIELD-STAR DECONTAMINATION*

Since the number of stars inside  $R = 75''$  is significantly affected by the background stellar population, statistical decontamination of the background field must be done. In this section we demonstrate that the observed SGB morphology is not caused by our approach to field-star decontamination. The method adopted for field-star decontamination is similar to that employed by [Li et al. \(2014b\)](#). We first used a Monte Carlo method to estimate the area of the region inside  $R = 75''$ . The fraction of the area inside this radius divided by the total area of the frame is 0.425.

We next counted the number of field stars in each color–magnitude bin and randomly deleted 0.425 times that number of stars from the corresponding color–magnitude bin of the CMD of the star cluster. If the number of stars that had to be removed from a bin was larger than the number of stars in the corresponding bin of the CMD of the cluster, we removed all stars in such a bin. In addition, we used a similar method to that adopted by [Cabrera-Ziri et al. \(2016\)](#) to estimate the significance of our field-star decontamination, where the signal-to-noise ratio is defined as the number of stars remaining in each color–magnitude bin after field-star decontamination divided by the average dispersion of the number of field stars in the corresponding bin. The significance levels of the color–magnitude bins adopted here are shown in Fig. 6 (left); the SGB region has been highlighted using red boxes. It is clear that the SGB region is characterized by a signal-to-noise ratio  $> 35$ . Specifically, any number from 0 to 5 stars must be removed from the 32 SGB stars in the blue region of the SGB,  $0.5 \leq (V - I) \leq 0.7$  mag, and 2 to 5 stars should be removed from the 34 stars occupying the red part of the SGB,  $0.7 \leq (V - I) \leq 0.89$  mag. The number of stars to be removed is much smaller, if not negligible, compared with the total number of stars located in those color ranges. Therefore, the SGB morphology is not affected significantly by our field-star decontamination. We confirmed that the field-decontamination quality is consistent for reasonable changes in bin sizes. Bin sizes that are too small will not result in adequate numbers of stars to be removed from a bin, while bin sizes that are too large will not allow us to distinguish the features of the field CMD from those of the cluster CMD.

The result of our field-star decontamination is shown in the middle and right-hand panels of Fig. 6. The top middle panel shows the CMD of the stars inside  $R = 75''$  in the cluster field. On the top right, we show the same cluster CMD, but after field-star decontamination. The bottom middle panel is the CMD of the entire field region, and the bottom right-hand panel is the CMD composed of stars that were randomly removed from the cluster region.

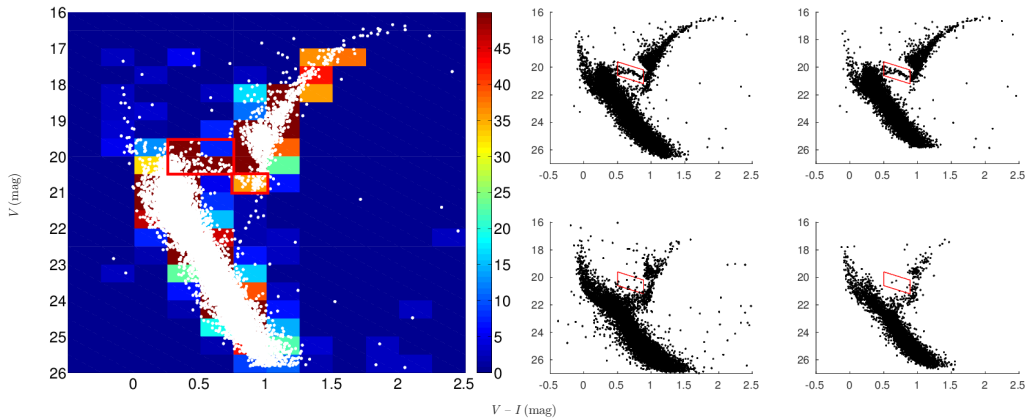


**Figure 6.** Left: CMD of the stars located within  $R = 75''$  from the cluster center after field star decontamination. Different colors represent different signal-to-noise ratios. The SGB region is highlighted with red boxes. Right: Field-star decontamination. Top middle: CMD of the cluster stars ( $R \leq 75''$ ). Top right: CMD of the cluster after field-star decontamination. Bottom middle: CMD of the entire field region. Bottom right: CMD of the randomly removed stars in the cluster field by our field-star decontamination procedure.

*STOCHASTIC VARIATIONS*

We constructed synthetic clusters to estimate the probability of not finding any old stars in the red part of the SGB because of stochastic effects. Using the SFH of the eMSTO and our set of model isochrones, we populated the main-sequence and SGB regions with stars randomly drawn from the ([Kroupa 2001](#)) stellar initial mass function. The numbers of stars of the synthetic clusters were normalized to the numbers of stars found in the main-sequence and SGB regions of the observed cluster CMD. We added unresolved binary companions to 50% of the stars located on the

main sequence (but none to the SGB stars), based on the observational  $\sim 20\%$  unresolved binary fraction, with mass ratio  $q \leq 0.6$ , assuming a flat mass-ratio distribution. We obtained this unresolved binary fraction using the method of Li et al. (2014a). It is close to that derived by Rubele et al. (2010), who found a binary fraction of  $\sim 18\%$  for mass ratios greater than 0.7. Photometric errors were added to the stars, and the simulations were run 1000 times. Each time we calculated two SFHs, for the blue and red parts of the SGB. Figure 7 shows the results of our simulations: the left-hand panel shows one typical synthetic cluster characterized by an age spread based on the extent of the eMSTO, while the right-hand panel illustrates the frequency of detecting a fraction  $P(N)$  of red SGB stars associated with the oldest isochrones, aged 1.82 Gyr, 1.92 Gyr, and 2.02 Gyr. The probability of not finding red SGB stars near the oldest isochrones is very small indeed. For instance, the frequency of finding fewer than 10% of red SGB stars near the oldest isochrones is  $P < 0.05$ . Therefore, stochastic variations are not responsible for the converging trend seen in the SGB of NGC 419.

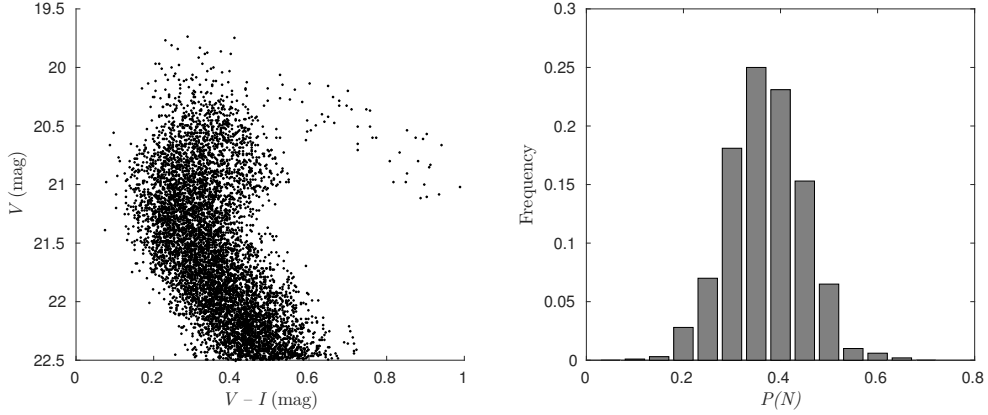


**Figure 7.** Left: example of a synthetic cluster realization. Right: detection probability,  $P(N)$ , of red SGB stars to be associated with the oldest isochrones adopted (1.82 Gyr, 1.92 Gyr, and 2.02 Gyr).